Topologically Enclosed Aluminium Voids as Plasmonic Nanostructures

Ye Zhu,[†,#,*] Philip N. H. Nakashima,[†] Alison M. Funston,[‡] Laure Bourgeois,[†,||] Joanne Etheridge,[†,||,*]

[†]Department of Materials Science and Engineering, Monash University, VIC 3800, Australia
[#]Department of Applied Physics, The Hong Kong Polytechnic University, Hung Hom, Kowloon, Hong Kong, P. R. China
[‡]ARC Centre of Excellence in Exciton Science, School of Chemistry, Monash University, VIC 3800, Australia
[||]Monash Centre for Electron Microscopy, Monash University, VIC 3800, Australia

*Corresponding author: email joanne.etheridge@monash.edu yezhu@polyu.edu.hk

KEYWORDS: *plasmonics, nanovoids, aluminium, electron energy-loss spectroscopy, electron-driven discrete-dipole approximation*

ABSTRACT

Recent advances in the ability to synthesise metallic nanoparticles with tailored geometries have led to a revolution in the field of plasmonics. However, studies of the important complementary system, an inverted nanostructure, have so far been limited to two-dimensional sphere-segment voids or holes. Here we reveal the localized surface plasmon resonances (LSPRs) of nanovoids that are topologically enclosed in three-dimensions: an "anti-nanoparticle". We combine this topology with the favourable plasmonic properties of aluminium to observe strongly localised field enhancements with LSPR energies in the extreme UV range, well beyond those accessible with noble metals or yet achieved with aluminium. We demonstrate the resonance tunability by tailoring the shape and size of the nanovoids, which are truncated-octahedra in the 10-20 nm range. This system is pristine: the nanovoid cavity is free from any oxide or supporting substrate that would affect the LSPRs. We exploit this to infer the LSPRs of pure, sub-20nm Al nanoparticles which have yet to be synthesized. Access to this extreme UV range will allow applications in LSPR-enhanced UV photoemission spectroscopy and photoionization.

The localized surface plasmon resonances (LSPRs) supported by metallic nanostructures play a central role in the fast-developing field of plasmonics. With advances in wet chemical synthesis and nanofabrication, metallic nanoparticles with various shapes, sizes, and

compositions can be produced, leading to highly tunable LSPRs and the associated local electromagnetic field enhancements.[1-3] Numerous applications have emerged including LSPR-enhanced spectroscopy and chemical sensing, as well as catalysis and optoelectronics.[1-5]

Considerable advances have been made in understanding the plasmonic response of nanoparticle systems, including the dependence of the plasmon resonance energy on the metal, as well as nanoparticle shape and size.[1-3] However, much less is known about the complementary system, an inverted nanostructure or "anti-nanoparticle".[6] Indeed, experimental studies have so far been limited to essentially two-dimensional (2D) systems (namely, holes or truncated spherical voids)[6-16] or dielectric spheres encapsulated in metal.[17] A topologically enclosed void (that is, an empty space containing no matter, completely encapsulated by a material) has not previously been studied experimentally, due to the difficulty of creating such fully-encapsulated voids.

Here we present the experimental LSPR study of topologically enclosed 3D nanovoids. These are grown and fully encapsulated within aluminium, as illustrated in Figure 1a and 1b. Aluminium is an attractive material for plasmonic applications due to its relative abundance and low cost (in contrast to the noble metals), combined with its tuneable high-energy LSPRs.[18-37] However, the fabrication and synthesis of Al nanostructures have presented a number of difficulties compared with their noble metal analogues, which has impeded its use in plasmonic nanostructures. For example, the plasmon linewidth of fabricated Al nanoparticles is large across the visible range due to damping by the interband transitions which occur at ~1.5 eV[21,38] plus surface roughness and grain boundaries within the particles.[32] Recently, a number of significant advances in Al plasmonics have been made. In particular, chemical synthesis of crystalline Al nanoparticles has been achieved, delivering nanoparticles >70 nm in diameter.[33] These have shown promise in UV-catalysis.[34] In addition, fabricated Al-based plasmonic devices have been engineered to reduce the plasmon linewidth and achieve highly sensitive, deep-UV surface enhanced Raman sensing,[27] colorimetric sensing,[35] and plasmonic-based displays.[36,37] Both fabricated and chemically synthesised Al nanoparticles oxidise, with oxide layers typically 2 – 4 nm, which is known to red-shift the energy of the LSPR.[22,31,33]

In the present work, nanovoids were grown within Al foils in the shape of truncated octahedra with sizes <20 nm (Figure 1b). The plasmonic response of these fully buried voids, and its dependence on size and shape, was investigated using electron energy-loss spectroscopy (EELS) in a scanning transmission electron microscope (STEM).[18,39-43] A key virtue of these

encapsulated internal voids is the absence of any supporting substrate or complicating oxide on the void surface, providing a pure system for fundamental studies. We exploit this and use the experimental measurements from nanovoids to derive, from the *sum rule*, the LSPR properties of pure Al nanoparticles <20 nm in diameter, which have yet to be reliably synthesised.[18-37] We also investigate a coupled void system with a view to future fabrication of coupled nanovoid arrays.

RESULTS AND DISCUSSION

The 3D nanovoids were fabricated by quenching high-purity aluminium (99.9999+ at.%) from a temperature just below its melting point. The Al nanovoids are {111}-terminated octahedra truncated by {100} planes at the six corners. Owing to the absence of mass, they appear darker in annular-dark-field (ADF) STEM images (inset, Figure 1c) for a <110>-oriented void. EEL spectra taken from different regions of the void show distinct peaks between 9 and 14 eV (Figure 1c and Supplementary Figure 1). There are no such peaks in the spectrum taken from the surrounding Al matrix (black curve, Figure 1c), indicating that they are associated with LSPRs of this inverted system. However, these peaks inevitably sit on the tails of the prominent bulk plasmon (~15 eV for Al) and the surface plasmon peaks of the oxidised Al film surfaces (7-8 eV). Subtracting the bulk-Al spectrum reveals three main energy-loss peaks when the electron beam is positioned at specific points across the void (Figure 1e). For the beam positioned at the {111} face centre (red square, inset, Figure 1c) a low energy peak ~11 eV dominates the loss signal. A higher energy signal is observed at ~12.5 eV for the beam positioned at the truncated-octahedral edge (green rectangle) and the highest energy peak at ~13 eV dominates the loss signal when the beam is positioned at the {100}-faceted corner (blue square).

These features of the EEL spectra are confirmed by electrodynamic EELS simulations based on the electron-driven discrete-dipole approximation (*e*-DDA),[44-46] as shown in Figure 1d and 1f (see also Supplementary Note 1 and Supplementary Figures 3-7). Both the raw experimental spectra and the bulk-Al-subtracted spectra are reproduced, demonstrating the power of the *e*-DDA calculations in describing both surface and bulk plasmon excitations. The calculations also reveal that the LSPR peaks are intrinsically broad, with FWHMs ≥ 1 eV (Figure 1f). It verifies that our instrumental resolution (~0.5 eV) is sufficient to characterize these peaks with little instrumental broadening (comparing Figure 1e with 1f). The broad nature of the LSPR peaks, together with the spatial overlap between the different LSPR modes, leads to

considerable signal mixing in both the experimental and calculated spectra. To separate the LSPR modes and to achieve spatially-resolved maps representing pure LSPR modes, we apply a multivariate analysis for blind decomposition (non-negative matrix factorization (NMF)),[43] summarized in Figure 2. Four distinct spectral components (three LSPR spectra and the bulk-Al spectrum) are separated robustly, which form a basis set to sufficiently model the raw spectra (bottom-left plot in Figure 2). In contrast to the mixed spectra (Figure 1e), each isolated LSPR component is dominated by a single peak (peak positions summarized in Table 1), suggesting a separation of the intrinsic plasmon modes. Furthermore, the NMF analysis as a function of beam position also allows the spatial distribution of each spectral component to be determined (middle panel, Figure 2). For the three major zone-axes of Al, the EELS spectra show no significant variations from different voids similar in size, and their spatial distributions are consistent: the red, green, and blue components localize at the {111} faces, edges, and {100}-faceted corners of voids, respectively. The mixed-color maps can be interpreted based on the ideal truncated-octahedral models in all three orientations.

The *e*-DDA calculated EELS maps at different resonance energies (right panel, Figure 2) show good agreement with experimental maps for the <100>-oriented void, further validating the spatial distributions of LSPR modes derived from NMF analysis. Similar spatial distributions of LSPR modes can also be obtained using principal-component analysis, but the derived spectral components can have non-physical negative intensities (Supplementary Figures 8-10). Figure 2 therefore provides a complete picture of the three prominent LSPR modes from nanovoids in Al in different orientations. These comprise a lower-energy {111} face mode; an intermediate-energy edge mode; and the highest energy mode localized at the {100}-faceted void corners. We note that the spatial spreads of all LSPR modes revealed here are $\leq$ 5 nm and are thus more localized than other reported LSPR modes.[39,42,43] This can be attributed to both the geometry of the truncated-octahedral nanovoids (*i.e.* perfectly flat facets and edges sharp at the nanometer scale[47]) and less delocalization of the higher energy-loss interactions with the incident electron beam.[48]

To gain greater physical insight into the origin of the LSPR signals, we calculate the induced electric field distributions in 3D for fixed electron beam positions and energy losses, (Figure 3). Despite the fixed beam positions, the induced field always spans the whole void, demonstrating the resonant nature of stationary waves excited by the incident electrons. The induced field is enhanced at the {111} faces (red), <110> edges (green), and {100}-faceted

corners (blue) of the voids for 10.7 eV, 12.1 eV and 13.2 eV, respectively - consistent with EELS maps for the corresponding LSPR modes (Figure 2). However, a careful inspection of Figure 3a reveals that the field enhancement for the "corner mode" is localized at the <110> edges surrounding the {100} facets, rather than at the {100} facets themselves (as seen for the "face mode" case), indicating that the "corner mode" in Figure 2 is actually another "edge mode" localized at the {100}-faceted corners.

The excellent agreement between experiments and calculations in Figs. 1-3 is conventionally difficult to achieve in Al plasmonics: Al plasmon resonances depend sensitively on surface oxidation, and granular structure, which are inevitable in Al nanoparticles.[19-33] These structural complexities in Al nanostructures often lead to discrepancies between experiments and theoretical predictions,[31] making the interpretation of Al plasmonic properties challenging. The exceptional agreement achieved here can be attributed to the purity of the nanovoid system: The voids have clean, oxide-free surfaces[47] and are embedded in large volumes of single crystal Al (hundreds of microns from grain boundaries). Importantly, there is no supporting substrate either. The nanovoids therefore provide a special system free of structural complexities, ideal for investigations of the intrinsic LSPR properties of aluminium.

We can exploit the purity of this nanovoid system to explore the LSPR response of the complementary nanoparticle system by applying the *sum rule*[16,49] to the experimentally measured nanovoid LSPRs. We demonstrate the validity of this approach by comparing these experimentally deduced LSPR energies with those determined from *e*-DDA calculations of pure Al nanoparticles with an identical truncated-octahedral geometry and size. By changing the electron beam positions relative to the nanoparticle in the calculation (Figure 4), all three major LSPR modes can be excited (consistent with the nanovoid system). The resonance energy for each mode is identical across particle orientations, with only the relative magnitudes of the loss probabilities changing, consistent with experimental observations of the nanovoid system (Figure 2).

Table 1 summarizes all resonance energies from both the nanovoid (measured experimentally) and the complementary nanoparticle systems (calculated using *e*-DDA). The resonance energies of the same mode from the two complementary systems (E_{s1}, E_{s2}) fulfil the *sum rule*[49]:

$$E_{s1}^2 + E_{s2}^2 = E_p^2$$

where E_p is the bulk plasmon energy (~15.3 eV for Al). This demonstrates that the plasmonic properties of pure (oxide and grain-boundary free) Al nanoparticles can be derived simply from experimental measurements of the complementary nanovoid system *via* the *sum rule*. We note that Al nanoparticles with shapes similar to truncated octahedra have been synthesised experimentally, but only with sizes >70 nm and with an oxide surface layer.[33]

Table 1. The *sum rule* of LSPR energies from Al nanovoids and nanoparticles with small {100} facets (d_{100} = 17 nm)

Truncated octahedra	**LSPR modes**		
small {100} (d_{100} = 17 nm)	**Face**	**Edge**	**Corner**
$\boldsymbol{E_{s1}}$: Al nanovoids (*experiment*)	10.7 eV	12.6 eV	13.3 eV
$\boldsymbol{E_{s2}}$: Al nanoparticles (*e-DDA*)	10.8 eV	8.9 eV	7.4 eV
$E_p = \sqrt{\boldsymbol{E_{s1}}^2 + \boldsymbol{E_{s2}}^2}$ = 15.3 eV	15.2 eV	15.4 eV	15.2 eV

It has been reported that the shape of Al nanovoids can be tailored using high-energy (≥160 kV) electron irradiation: the {100} facets move towards each other (d_{100} decreases) while the {111} facets remain fixed, giving rise to larger {100} facets.[47] STEM-EELS mapping of large-{100} faceted voids reveals that this shape modification can effectively tune the corner-mode peak from 13.3 to 12.7 eV, combined with a subtle redshift of the face-mode peak, (Figures 5a and 5b and Supplementary Figures 1 and 2). *e*-DDA simulations (Figures 5c and 5d) confirm the experimental observation and further show that, by tailoring the void shape from a perfect octahedron (d_{100} = 20 nm, dashed curves) to a large-{100} truncated octahedron (d_{100} = 14 nm, dotted curves), the corner-mode peak redshifts from 13.6 to 12.7 eV (Figure 6a).

The opposite trend was observed in the simulation of the complementary Al nanoparticle systems: changing the shape from an octahedron to a large-{100} truncated octahedron blueshifts the corner-mode peak from 6.6 to 8.3 eV (Figure 6d and Supplementary Figure 11). This is again consistent with the *sum rule*: the corner-mode energies from complementary systems with the same shape fulfil the *sum rule*, as demonstrated in Table 2. Again, this

demonstrates that the LSPR energies for the yet-to-be-synthesised nanoparticles can be determined accurately from the experimental measurements of the nanovoids *via* the *sum rule.*

Table 2. The *sum rule* of corner-mode LSPR energies from the Al nanovoids and nanoparticles with different shapes. Experimentally measured energy values are indicated by "*exp*", all other values are derived from *e*-DDA calculations.

	Corner mode		
Truncated octahedra (d_{111}=12 nm)	large {100} (d_{100} = 14 nm)	small {100} (d_{100} = 17 nm)	no {100} (d_{100} = 20 nm)
$\boldsymbol{E_{s1}}$: Al nanovoids	12.7 eV (*exp*)	13.3 eV (*exp*)	13.6 eV
$\boldsymbol{E_{s2}}$: Al nanoparticles	8.3 eV	7.4 eV	6.6 eV
$E_p = \sqrt{\boldsymbol{E_{s1}}^2 + \boldsymbol{E_{s2}}^2}$ = 15.3 eV	15.2 eV	15.2 eV	15.1 eV

It is worth pointing out that for the large-{100} faceted void (d_{100} = 14 nm), the corner-mode peak at 12.7 eV is nearly identical to the edge-mode peak, as shown by the blue and green curves in Figure 5d (also indicated by the arrows in Figures 6a,b). Induced electric field calculations (Figure 3c) also show that both modes exhibit similar field enhancements at the {110} edges. They confirm the observation in Figure 3a, that the corner mode is actually another "edge mode" localized at the {100}-faceted corners. Furthermore, a comparison between Figures 3a and 3c suggests that the corner and edge modes become degenerate when the {110} edges all have the same length, as seen in the large-{100} faceted void. When the {110} edges become shorter around the corners, as for the small-{100} faceted void, the corner mode is split from the edge mode (at 12.6-12.7 eV) and shifts towards higher energy, which was observed experimentally (Figure 5a,b). The same trend was observed in the Al nanoparticle systems (indicated by arrows in Figures 6d,e). A blue-shift of resonance energy with an increase in the degree of truncation of nanocrystals is consistent with that predicted for triangular prisms[50] and observed experimentally for decahedra.[51] Our calculations give a physical justification for these reported empirical observations.

We also explored the coupling effects between adjacent voids in analogy to complementary nanoparticle dimers. The possibility for these voids to grow in close proximity to each other, as observed in our sample (Figure 7b), suggests the potential for controlled nucleation and growth of coupled nanovoid systems. We explore the usefulness of this for plasmonic enhancement using *e*-DDA and find that weak plasmonic coupling of Al nanovoids separated by ~1.6 nm is possible (Figure 7c). A broad peak at 10.4 eV is likely due to the dark-mode resonance from coupling, as the resonance energy is lower than all the plasmonic modes from a single void. For the experimentally observed voids (Figure 7a,b), the lateral separation is observed to be a single atomic layer (~0.3 nm), but the depth separation in this particular case is determined to be 6 nm using quantitative convergent-beam electron diffraction (QCBED, see Methods) taken through each void, therefore no coupling between these two voids was observed in the EELS measurements. Further investigation on the production of nanovoid dimers and arrays that are sufficiently close to enable coupling is underway.

As a final remark, the overall shape of a void is defined by the lowest energy crystallographic planes of the host matrix, here aluminium. Very little is known regarding the mechanisms of void nucleation and growth, and there exists as yet no method for the arbitrary control of shape and size. However, some control has been demonstrated, as outlined in Methods, suggesting opportunities for future exploitation. In addition, voids can be fabricated in much larger number densities and as ordered arrays through ion beam irradiation.[52,53] This offers the prospect of fabricating arrays of voids in chosen patterns to engineer desired photonic behaviour.

CONCLUSION

In summary, we demonstrate that these tiny, aluminium-encapsulated 3D nanovoids provide strongly localized field enhancements with tuneable LSPR energies that extend the currently available plasmon spectrum into the extreme UV region. These energies are far beyond that achievable with noble metal nanoparticles and are equal or greater than would occur in the complementary aluminium nanoparticle system - if it could be synthesized. This is a pure and simple system, free from oxides, defects and substrates, and hence ideal for studying the intrinsic properties of Al plasmonics *via* the *sum rule*. Moreover, the potential to control the nucleation and growth of these nanovoids and the weak field enhancement associated with coupled nanoparticles, open the possibility of engineering useful and cheap plasmonic nanovoid arrays for applications requiring the extreme UV regime.

METHODS

Truncated octahedral voids were made reproducibly with diameters ranging from sub-10 nm to ~25 nm as well as with varying aspect ratios. This was achieved through different heat treatments involving heating high-purity aluminium (99.9999+ at.%) to just below its melting point (typically 550-600°C), in order to generate a high equilibrium vacancy population, and then quenching at different rates and temperatures in order to manipulate the clustering of vacancies into voids. Quenching was performed into 0°C and 20°C water as well as into liquid nitrogen. STEM imaging and EELS mapping were carried out on a double-Cs corrected FEI Titan 80-300 S/TEM equipped with a Gatan Image Filter (GIF Tridiem), operating at 80 kV and with a standard Schottky field emission gun (FEG) *without* a monochromator. The lower accelerating voltage causes less damage in bulk Al,[54,55] which is essential to achieving reliable EELS mapping on voids but still provides sufficient energy for the electrons to be transmitted through the full thickness of the foil. The electron gun lens setting was adjusted to reduce the beam current, so that the EELS energy resolution could be improved to ~0.5 eV (from 0.8-0.9 eV for a Schottky FEG) as measured from the FWHM of the zero-loss peak. The energy resolution can be further enhanced by post-processing using the Richardson-Lucy deconvolution.[56] A ~18 mrad convergence angle was used to yield a ~2 Å diameter electron beam, and a ~10 mrad collection angle was used to collect the EEL signal. To exclude any beam damage artefacts, we monitored the STEM images carefully to make sure that there were no structural changes after EELS mapping. Multiple EELS mapping on the same voids was also performed to check for consistency. To compare with experimental observations, electrodynamic EELS simulations were performed based on the electron-driven discrete-dipole approximation (*e*-DDA),[44-46] with the simulation parameters presented in Supplementary Note 1. To determine the void geometry and dimensions, convergent-beam electron diffraction (CBED) patterns were also collected with the electron beam traversing a void and were pattern-matched using the 'multislice' description of electron scattering.[57] The void was modelled as a sequence of slices that contain no atoms, sandwiched by two pure Al slabs. Such a quantitative CBED (QCBED) approach can determine the dimension of a void along the direction of the incident beam with a precision of 3 atomic layers. The accuracy and precision of the QCBED measurements is unaffected by the presence of amorphous oxide layers at the top and bottom exterior surfaces of the TEM foil, the effect of which is removed through the differential QCBED analysis.[58-60]

ASSOCIATED CONTENT

The Supporting Information containing additional experimental data, data analysis, and details of simulations is available free of charge on the ACS Publications website at DOI:

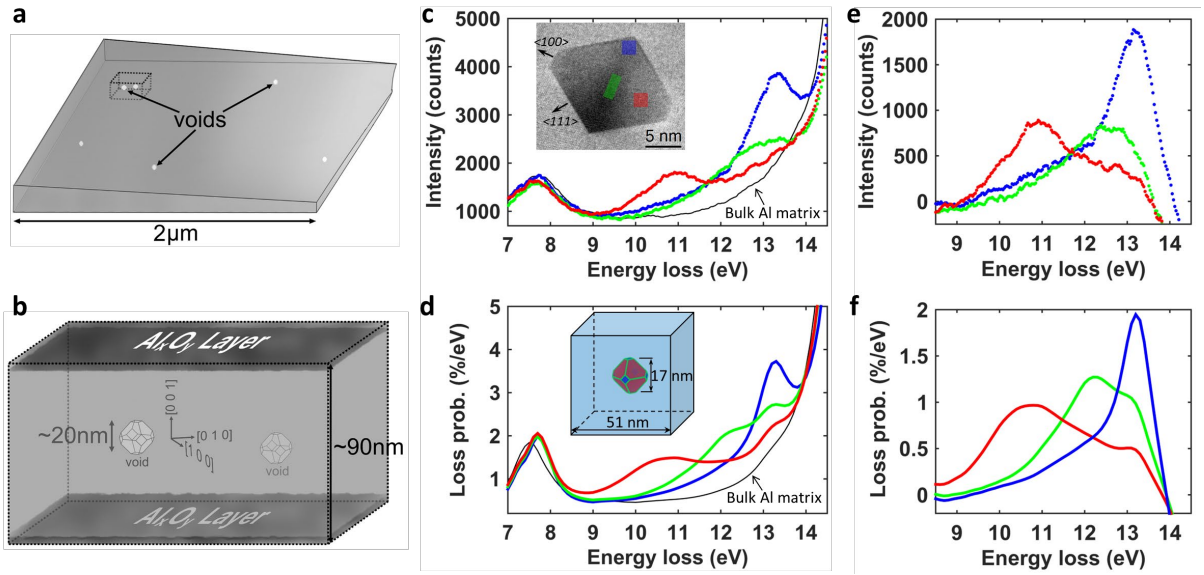

Figure 1. EEL spectrum comparison between experiments and calculations. (a) A schematic showing voids fully enclosed in a TEM specimen of an Al foil. (b) A magnified rectangle from (a) showing two truncated-octahedral voids inside an Al foil with thin AlO_x layers above and below. (c) Experimental EEL spectra corresponding to regions highlighted in the inset. Inset: ADF-STEM image showing a void with truncated octahedral shape in <110>-oriented bulk Al. (d) *e*-DDA calculated spectra at the face (red), edge (green), and corner (blue) of a truncated-octahedral void. Inset: model used for calculation, showing a void with d_{100} ~17 nm embedded in a 51 nm Al cube. The Al cube is covered by a ~3 nm Al_2O_3 surface oxidation layer. (e,f) Net spectra after subtracting the bulk Al spectra from (e) the experiment and (f) the calculation.

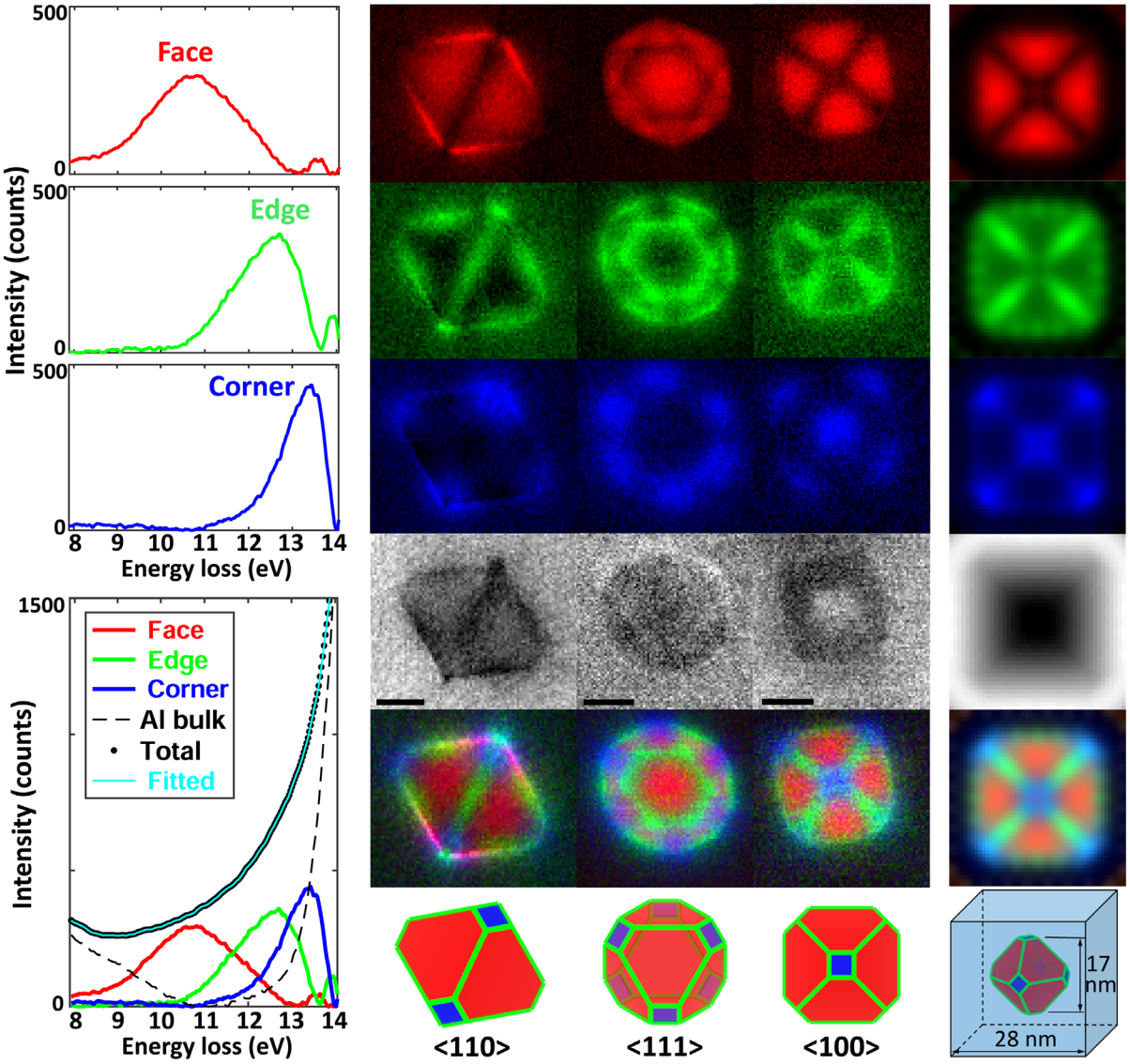

Figure 2. STEM-EELS mapping of LSPRs on three Al nano-voids in multiple projections. **Left panel:** The component spectra derived from NMF analysis. Bottom-left plot shows a raw EEL spectrum (black dots) averaged over a whole void. The spectrum can be perfectly fitted (cyan curve) with the four components derived from NMF analysis. **Middle panel:** The EELS weight maps associated with the component spectra on the left, illustrating the spatial distribution of the face (top row, red), edge (2nd row, green), and corner (3rd row, blue) modes in different orientations. **4th row:** Weight maps formed by the Al bulk spectrum (dashed curve in the bottom-left plot), showing "bright-field" STEM contrast. Scale bars equal 5 nm. **5th row:** False-color mixed maps are in excellent agreement with the truncated octahedral models (bottom row). **Right panel,** *e*-DDA calculated EELS maps for a void with d_{100} ~17 nm embedded in a 28 nm oxide-coated Al cube. The non-uniform EELS intensity along <110> for the edge mode (green) is a simulation artefact due to the limited number of dipoles used to model the void.

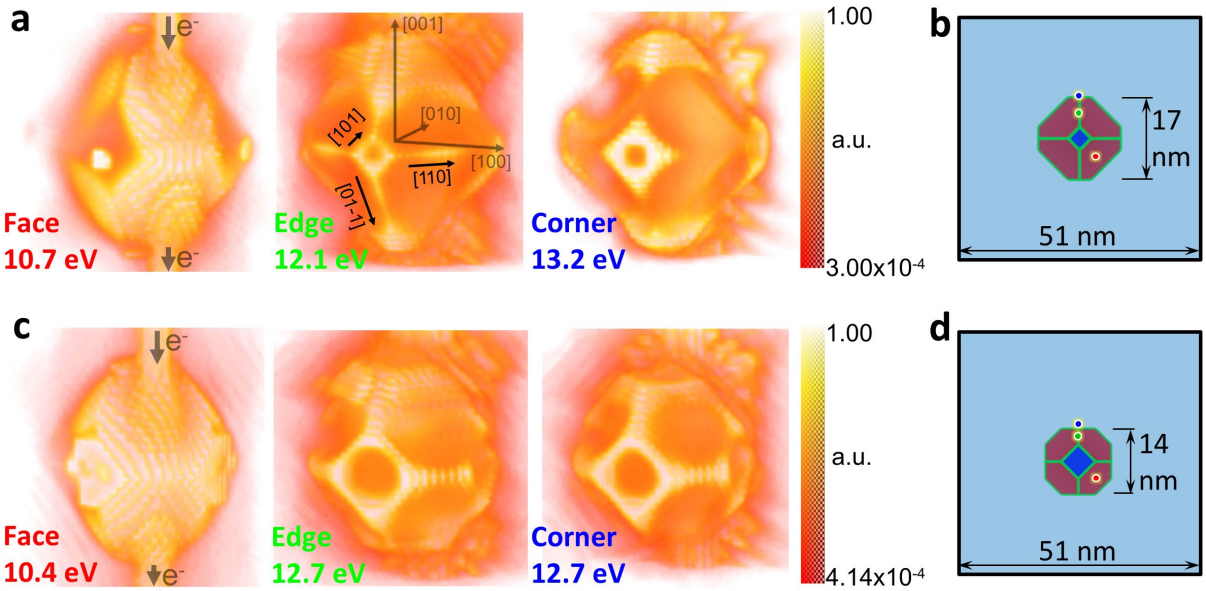

Figure 3. (a) *e*-DDA calculated E^2 plot in 3D. Both the induced electric fields and the electron beam path along <100> light up. The scale is normalized to the maximum E^2 and is therefore dimensionless (same for c). Crystallographic axes are drawn to show void orientation in the middle panel and the directions of some of the bounding edges are also indicated. Note that all edges bounding voids in aluminium have <110> orientations. The LSPR modes and corresponding resonance energies are labelled at the lower-left corner. Energies slightly off the resonance energies are used to minimize the mixing effects from different LSPR modes. (b) Model used for calculations (same model used in Figure 1b,d). Dots show the electron beam positions which excite face (red), edge (green) and corner (blue) LSPR modes. (c) *e*-DDA calculated E^2 plot in 3D, the same as (a) but for a void with larger {100} facets. (d) Model used for calculations in **c** showing a void with d_{100} ~14 nm embedded in the same cube as (b). Note that the model in (d) has the same d_{111} as in (b), but smaller d_{100} due to a larger truncation.

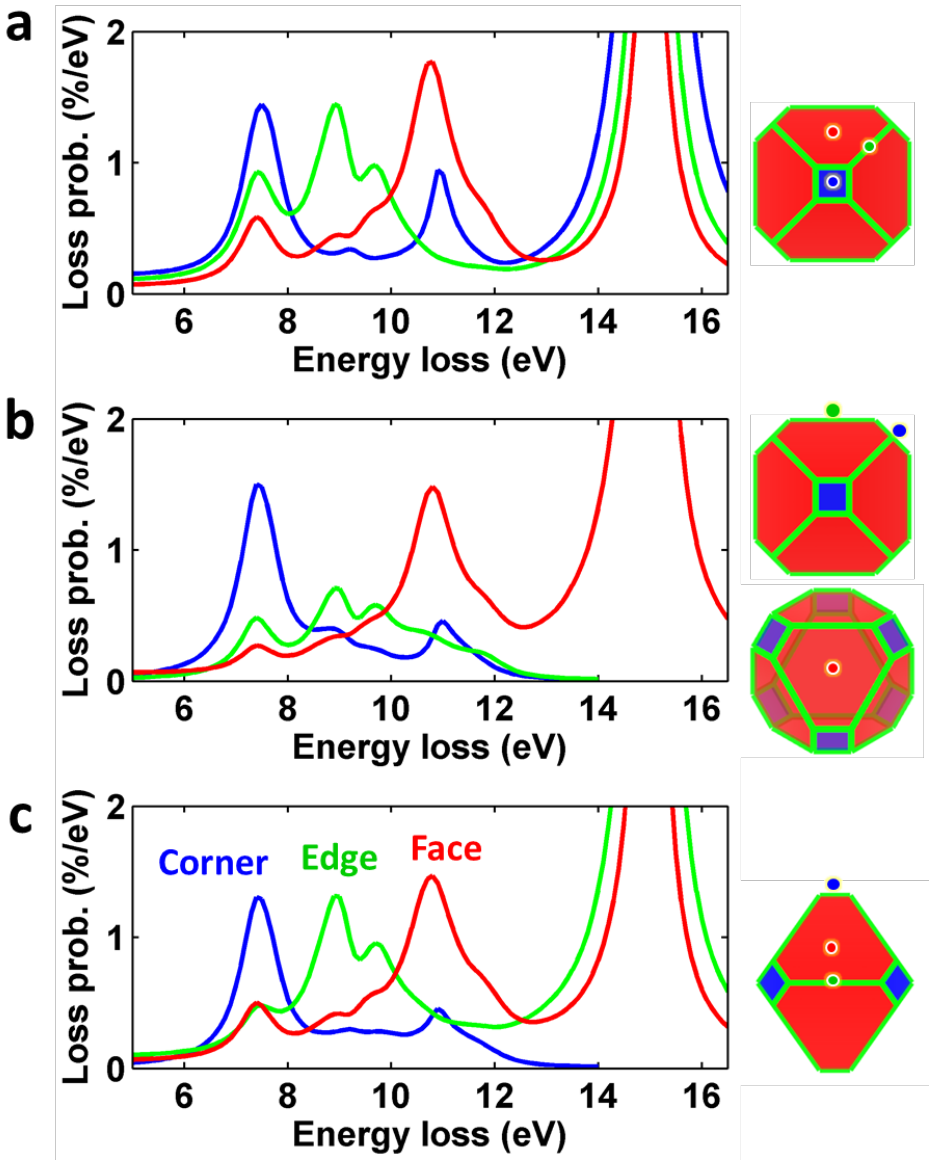

Figure 4. *e*-DDA calculated EEL spectra for an Al nanoparticle with a truncated octahedral shape and d_{100} ~17 nm. (a-c) Spectra from (a) a <100>-oriented particle, (b) <100>- and <111>-oriented particles, (c) a <110>-oriented particle, with electron beam positions indicated by dots in the corresponding colors on the right. The color scheme: blue, green, and red are for the corner, edge, and face LSPR modes, respectively. The LSPR peak positions are insensitive to the nanoparticle orientation (with respect to the electron beam direction). Also note that the bulk-plasmon peak is absent when the electron beam is outside the particle.

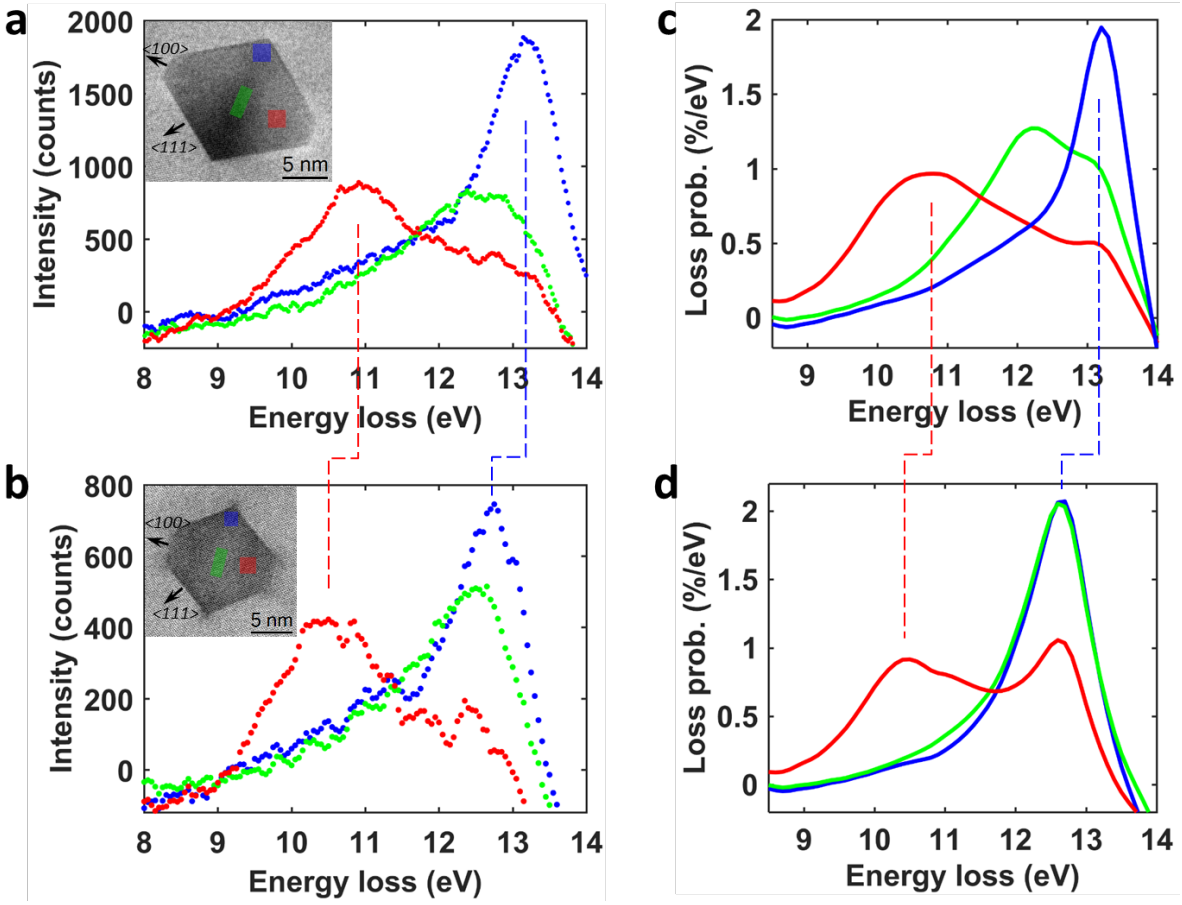

Figure 5. Tunability of LSPR modes with the shape of Al nano-voids. (a,b) Experimental net spectra after subtracting the bulk Al spectra from voids with (a) small- and (b) large-{100} faceted corners. Insets: ADF-STEM images showing the corresponding voids in <110>-oriented bulk Al regions where EEL spectra are taken highlighted. (c,d) Calculated net spectra after subtracting the bulk Al spectra from (c) small- and (d) large-{100} faceted voids. The dashed lines illustrate the redshifts of the LSPR peaks from face (red) and corner (blue) modes from small- to large-{100}-faceted voids, for experiments and calculations. (a) and (c) present the same data as Figs. 1e and 1f.

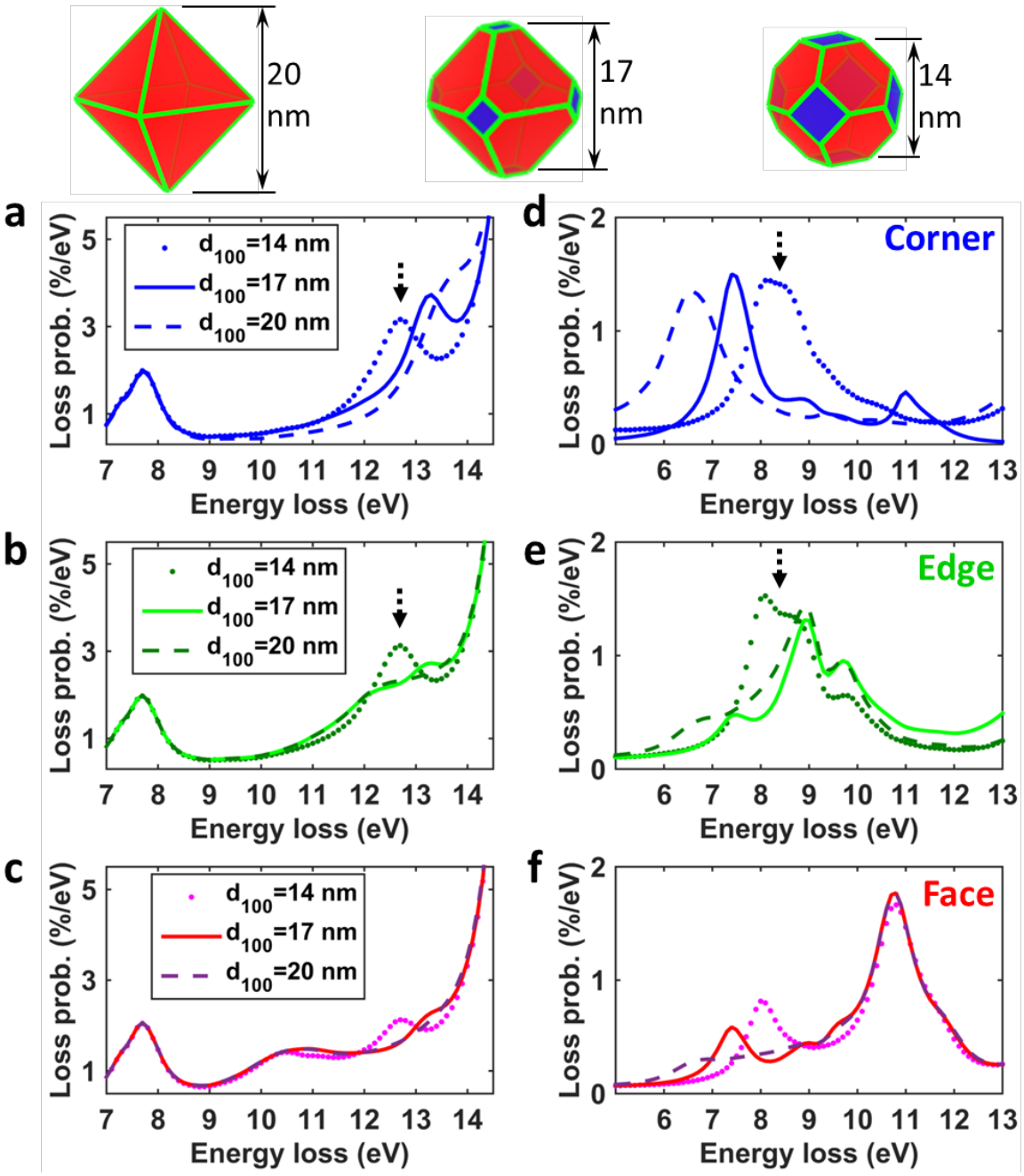

Figure 6. Tunability of LSPR modes with the shape of Al nano-voids and nanoparticles. (a-c) *e*-DDA calculated EEL spectra for the (a) corner mode, (b) edge mode, and (c) face mode, from voids with different shapes as indicated by the models on top. All voids have d_{111} fixed to be 12 nm, with the shape change controlled by d_{100}. All voids are embedded in a 51 nm Al cube covered by a ~3 nm Al_2O_3 surface oxidation layer. (d-f) *e*-DDA calculated EEL spectra for the (d) corner mode, (e) edge mode, and (f) face mode, from nanoparticles that are complementary to each of the nano-voids in (a-c) (*i.e.* they have the same shapes). See Supplementary Figure 11 for optical DDSCAT calculations using a photon source on these nanoparticles.

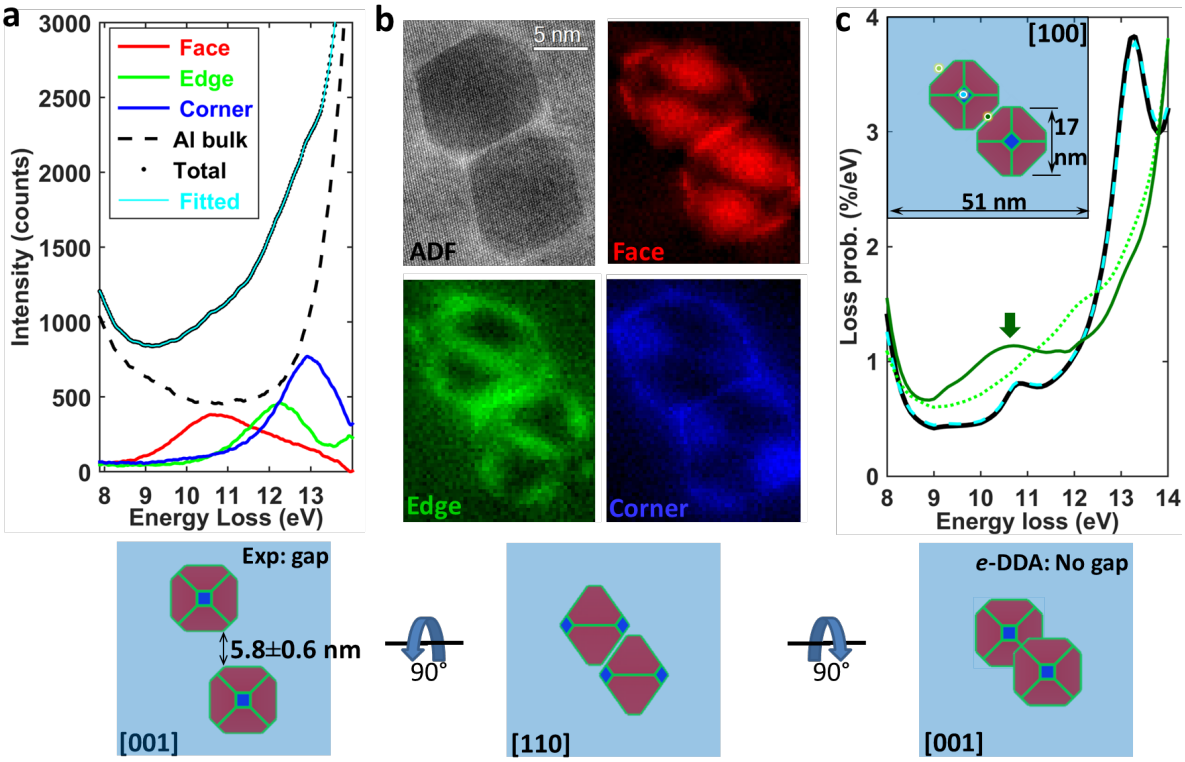

Figure 7. STEM-EELS mapping of LSPRs from two voids close to each other. (a) Raw EEL spectrum (black dots) averaged over the whole mapping area. The spectrum can be fitted perfectly (cyan curve) with the four components derived from NMF, but show no signature of void coupling. (b) ADF-STEM image and EELS weight maps associated with the component spectra in (a), illustrating the spatial distribution of the face (red), the edge (green), and the corner (blue) modes along the <110> zone axis. (c) *e*-DDA calculated EEL spectra for an edge-to-edge void dimer with 1.6 nm distance between the two closest edges. The inset shows the model used for calculations at the [100] zone axis, with the cyan, light-green, and dark-green dots indicating the electron beam positions for the correspondingly-colored EEL spectra. The thick black spectrum is from the single void calculation, which is nearly identical to the dashed cyan spectrum from the void dimer calculation, indicating very weak coupling. On the other hand, a broad peak at ~10.4 eV in the dark-green spectrum (indicated by an arrow) is likely to reflect the dark-mode resonance from coupling. Such a weak coupling is not observed experimentally in (a) and (b), due to the ~6 nm separation between the two voids along the [110] direction, as illustrated in the bottom-left model. The model of an edge-to-edge void dimer (*i.e.* no gap, used in the *e*-DDA calculation) is shown in the bottom right, while both models look the same in the [110] orientation.

TABLES

Table 1. The *sum rule* of LSPR energies from Al nanovoids and nanoparticles with small {100} facets (d_{100} = 17 nm)

Truncated octahedra	**LSPR modes**		
small {100} (d_{100} = 17 nm)	**Face**	**Edge**	**Corner**
$\boldsymbol{E_{s1}}$: Al nanovoids (*experiment*)	10.7 eV	12.6 eV	13.3 eV
$\boldsymbol{E_{s2}}$: Al nanoparticles (*e-DDA*)	10.8 eV	8.9 eV	7.4 eV
$E_p = \sqrt{\boldsymbol{E_{s1}}^2 + \boldsymbol{E_{s2}}^2}$ = 15.3 eV	15.2 eV	15.4 eV	15.2 eV

Table 2. The *sum rule* of corner-mode LSPR energies from the Al nanovoids and nanoparticles with different shapes. Energies are mostly derived from *e*-DDA calculations, with the experimental values indicated by "exp".

	Corner mode		
Truncated octahedra (d_{111}=12 nm)	large {100} (d_{100} = 14 nm)	small {100} (d_{100} = 17 nm)	no {100} (d_{100} = 20 nm)
$\boldsymbol{E_{s1}}$: Al nanovoids	12.7 eV (exp)	13.3 eV (exp)	13.6 eV
$\boldsymbol{E_{s2}}$: Al nanoparticles	8.3 eV	7.4 eV	6.6 eV
$E_p = \sqrt{\boldsymbol{E_{s1}}^2 + \boldsymbol{E_{s2}}^2}$ = 15.3 eV	15.2 eV	15.2 eV	15.1 eV

AUTHOR INFORMATION

Corresponding Author

*J. Etheridge email: joanne.etheridge@monash.edu

*Y. Zhu email: yezhu@polyu.edu.hk

Acknowledgements

The authors thank Dr Nicholas Bigelow and Prof David Masiello for helpful advice regarding their *e*-DDA code, A/Prof Matthew Weyland for optimizing the Titan microscope to achieve 0.5 eV energy resolution at 80 kV, and Prof Javier Garcia de Abajo and Dr Toon Coenen for helpful discussions. This work was supported by the Australian Research Council (ARC) grants numbers DP150104483 (JE), FT110100427 (PNHN), FT110100545 and CE170100026 (AMF), DP150100558 (LB), the Hong Kong Research Grants Council through the Early Career Scheme (Project No. 25301617) and the Hong Kong Polytechnic University grant (Project No. 1-ZE6G).The FEI Titan^3 80-300 FEG-TEM at the Monash Centre for Electron Microscopy was funded by ARC Grant LE0454166.

References

[1] Lal, S.; Link, S.; Halas, N. J. Nano-Optics from Sensing to Waveguiding. *Nature Photon.* **2007**, *1*, 641-648.

[2] Murray, W. A.; Barnes, W. L. Plasmonic Materials. *Adv. Mater.* **2007**, *19*, 3771-3782.

[3] Stockman, M. I. Nanoplasmonics: Past, Present, and Glimpse into Future. *Opt. Express* **2011**, *19*, 22029–22106.

[4] Anker, J. N.; Hall, W. P.; Lyandres, O.; Shah, N. C.; Zhao, J.; van Duyne, R. P. Biosensing with Plasmonic Nanosensors. *Nature Mater.* **2008**, *7*, 442–453.

[5] Schuller, J. A.; Barnard, E. S.; Cai, W.; Jun, Y. C.; White, J. S.; Brongersma, M. L. Plasmonics for Extreme Light Concentration and Manipulation. *Nature Mater.* **2010**, *9*, 193-204.

[6] Cole, R. M.; Baumberg, J. J.; Garcia de Abajo, F. J.; Mahajan, S.; Abdelsalam, M.; Bartlett, P. N. Understanding Plasmons in Nanoscale Voids. *Nano Lett.* **2007**, *7*, 2094-2100.

[7] Coyle, S.; Netti, M. C.; Baumberg, J. J.; Ghanem, M. A.; Birkin, P. R.; Bartlett, P. N.; Whittaker, D. M. Confined Plasmons in Metallic Nanocavities. *Phys. Rev. Lett.* **2001**, *87*, 176801.

[8] Murray, W. A.; Astilean, S.; Barnes, W. L. Transition from Localized Surface Plasmon Resonance to Extended Surface Plasmon-Polariton as Metallic Nanoparticles Merge to Form a Periodic Hole Array. *Phys. Rev. B* **2004**, *69*, 165407.

[9] Teperik, T. V.; Popov, V. V.; García de Abajo, F. J. Void Plasmons and Total Absorption of Light in Nanoporous Metallic Films. *Phys. Rev. B* **2005**, *71*, 085408.

[10] Kelf, T. A.; Cole, R. M.; Baumberg, J. J.; Abdelsalam, M. E.; Cintra, S.; Mahajan, S.; Russell, A. E.; Bartless, P. N. Localized and Delocalized Plasmons in Metallic Nanovoids. *Phys. Rev. B* **2006**, *74*, 245415.

[11] Romero, I.; Teperik, T. V.; Garcia de Abajo, F. J. Plasmon Molecules in Overlapping Nanovoids. *Phys. Rev. B* **2008**, *77*, 125403.

[12] Alù A.; Engheta, N. Comparison of Waveguiding Properties of Plasmonic Voids and Plasmonic Waveguides. *J. Phys. Chem. C.* **2010**, *114*, 7462-7471.

[13] Talebi, N.; Ögüt, B.; Sigle, W.; Vogelgesang, R.; van Aken, P. A. On the Symmetry and Topology of Plasmonic Eigenmodes in Heptamer and Hexamer Nanocavities. *Appl. Phys. A* **2014**, *116*, 947-954.

[14] Sigle, D. O.; Perkins, E.; Baumberg, J. J.; Mahajan, S. Reproducible Deep-UV SERRS on Aluminum Nanovoids. *J. Phys. Chem. Lett.* **2013**, *4*, 1449-1452.

[15] Schmidt, M.; Tognalli, N. G.; Otte, M. A.; Alonso, M. I.; Sepúlveda, B.; Fainstein, A.; Goñi, A. R. Spatial Distribution of Optical Near-Fields in Plasmonic Gold Sphere Segment Voids. *Plasmonics* **2013**, *8*, 921-930.

[16] Coenen, T.; Polman A. Optical Properties of Single Plasmonic Holes Probed with Local Electron Beam Excitation. *ACS Nano* **2014**, *8*, 7350–7358.

[17] Kho, K. W.; Shen, Z. X.; Olivo, M. Sub-Micron Free-Standing Metal Slabs with Dielectric Nano-Voids of Arbitrary Shapes Embedded beneath Atomically-Flat Surface. *Opt. Express* **2011**, *19*, 10518-10535.

[18] Batson, P. E. Surface Plasmon Coupling in Clusters of Small Spheres. *Phys. Rev. Lett.* **1982**, *49*, 936-940.

[19] Stöckli, T.; Bonard, J.-M.; Stadelman, P.-A.; Chatelain, A. EELS Investigation of Plasmon Excitations in Aluminum Nanospheres and Carbon Nanotubes. *Z. Phys. D: At., Mol. Clusters* **1997**, *40*, 425.

[20] Ekinci, Y.; Solak, H. H.; Löffler J. F. Plasmon Resonances of Aluminium Nanoparticles and Nanorods. *J. Appl. Phys.* **2008**, *104*, 083107.

[21] Langhammer, C.; Schwind, M.; Kasemo, B.; Zorić, I. Localized Surface Plasmon Resonances in Aluminum Nanodisks. *Nano Lett.* **2008**, *8*, 1461–1471.

[22] Chan, G. H.; Zhao, J.; Schatz, G. C.; Van Duyne, R. P. Localized Surface Plasmon Resonance Spectroscopy of Triangular Aluminium Nanoparticles. *J. Phys. Chem. C* **2008**, *112*, 13958−13963.

[23] Chowdhury, M. H.; Ray, K.; Gray, S. K.; Pond, J.; Lakowicz, J. R. Aluminum Nanoparticles as Substrates for Metal-Enhanced Fluorescence in the Ultraviolet for the Label-Free Detection of Biomolecules. *Anal. Chem.* **2009**, *81*, 1397-1403.

[24] Zorić, I.; Zach, M.; Kasemo, B.; Langhammer, C. Gold, Platinum, and Aluminum Nanodisk Plasmons: Material Independence, Subradiance, and Damping Mechanisms. *ACS Nano* **2011**, *5*, 2535–2546.

[25] Castro-Lopez, M.; Brinks, D.; Sapienza R.; van Hulst, N. F. Aluminum for Nonlinear Plasmonics: Resonance-Driven Polarized Luminescence of Al, Ag, and Au Nanoantennas. *Nano Lett.* **2011**, *11*, 4674-4678.

[26] Knight, M. W.; Liu, L.; Wang, Y.; Brown, L.; Mukherjee, S.; King, N. S.; Everitt, H. O.; Nordlander, P.; Halas, N. J. Aluminum Plasmonic Nanoantennas. *Nano Lett.* **2012**, *12*, 6000-6004.

[27] Jha, S. K.; Ahmed, Z.; Agio, M.; Ekinci Y.; Löffler, J. F. Deep-UV Surface-Enhanced Resonance Raman Scattering of Adenine on Aluminum Nanoparticle Arrays. *J. Am. Chem. Soc.* **2012**, *134*, 1966-1969.

[28] Hu, J.; Chen, L.; Lian, Z.; Cao, M.; Li, H.; Sun, W.; Tong, N.; Zeng, H. Deep-Ultraviolet–Blue-Light Surface Plasmon Resonance of Al and Al Core/Al_2O_3 Shell in Spherical and Cylindrical Nanostructures. *J.. Phys. Chem. C* **2012**, *116*, 15584–15590.

[29] Martin, J.; Proust, J.; Gérard, D.; Plain, J. Localized Surface Plasmon Resonances in the Ultraviolet from Large Scale Nanostructured Aluminum Films. *Opt. Mater. Express* **2013**, *3*, 954-959.

[30] Maidecchi, G.; Gonella, G.; Zaccaria, R. P.; Moroni, R.; Anghinolfi, L.; Giglia, A.; Nannarone, S.; Mattera, L.; Dai, H.-L.; Canepa, M.; Bisio, F. Deep Ultraviolet Plasmon Resonance in Aluminium Nanoparticle Arrays. *ACS Nano* **2013**, *7*, 5834-5841.

[31] Knight, M. W.; King, N. S.; Liu, L.; Everitt, H. O.; Nordlander, P.; Halas, N. J.Aluminum for Plasmonics. *ACS Nano* **2014**, *8*, 834-840.

[32] Liu, H.-W.; Lin, F.-C.; Lin, S.-W.; Wu, J.-Y.; Chou, B.-T.; Lai, K.-J.; Lin, S.-D.; Huang, J.-S. Single-Crystalline Aluminum Nanostructures on a Semiconducting GaAs Substrate for Ultraviolet to Near-Infrared Plasmonics. *ACS Nano* **2015**, *9*, 3875–3886.

[33] McClain, M. J.; Schlather, A. E.; Ringe, E.; King, N. S.; Liu, L.; Manjavacas, A.; Knight, M. W.; Kumar, I.; Whitmire, K. H.; Everitt, H. O.; Nordlander, P.; Halas, N. J. Aluminum Nanocrystals. *Nano Lett.* **2015**, *15*, 2751-2755.

[34] Zhou, L.; Zhang, C.; McClain, M. J.; Manjavacas, A.; Krauter, C. M.; Tian, S.; Berg, F.; Everitt, H. O.; Carter, E. A.; Nordlander, P.; Halas, N. J.Aluminum Nanocrystals as a Plasmonic Photocatalyst for Hydrogen Dissociation. *Nano Lett.* **2016**, *16*, 1478–1484.

[35] King, N. S.; Liu, L.; Yang, X.; Cerjan, B.; Everitt, H. O.; Nordlander, P.; Halas, N. J. Fano Resonant Aluminum Nanoclusters for Plasmonic Colorimetric Sensing. *ACS Nano* **2015**, *9*, 10628–10636.

[36] Olson, J.; Manjavacas, A.; Basu, T.; Huang, D.; Schlather, A. E.; Zheng, B.; Halas, N. J.; Nordlander, P.; Link, S. High Chromaticity Aluminum Plasmonic Pixels for Active Liquid Crystal Displays. *ACS Nano* **2016**, *10*, 1108–1117.

[37] Olson, J.; Manjavacas, A.; Liu, L.; Chang, W.-S.; Foerster, B.; King, N. S.; Knight, M. W.; Nordlander, P.; Halas, N. J.; Link, S. Vivid, Full-Color Aluminum Plasmonic Pixels. *Proc. Natl. Acad. Sci. U. S. A.* **2014**, *111*, 14348–14353.

[38] McPeak, K. M.; Jayanti, S. V.; Kress, S. J. P.; Meyer, S.; Iotti, S.; Rossinelli, A.; Norris D. J. Plasmonic Films Can Easily be Better: Rules and Recipes, *ACS Photonics* **2015**, *2*, 326-333.

[39] Nelayah, J.; Kociak, M.; Stéphan, O.; Garcia de Abajo, F. J.; Tencé, M.; Henrard, L.; Taverna, D.; Pastoriza-Santos, I.; Liz-Marzán, L. M.; Colliex, C. Mapping Surface Plasmons on a Single Metallic Nanoparticle. *Nature Phys.* **2007**, *3*, 348–353.

[40] Bosman, M.; Keast, V. J.; Watanabe, M.; Maaroof, A. I.; Cortie, M. B. Mapping Surface Plasmons at the Nanometre Scale with an Electron Beam. *Nanotechnology* **2007**, *18*, 165505.

[41] García de Abajo F. J.; Kociak, M. Probing the Photonic Local Density of States with Electron Energy Loss Spectroscopy. *Phys. Rev. Lett.* **2008**, *100*, 106804.

[42] Rossouw, D.; Couillard, M.; Vickery, J.; Kumacheva, E.; Botton, G. A. Multipolar Plasmonic Resonances in Silver Nanowire Antennas Imaged with a Subnanometer Electron Probe. *Nano Lett.* **2011**, *11*, 1499–1504.

[43] Nicoletti, O.; de la Pena F.; Leary, R. K.; Holland, D. J.; Ducati, C.; Midgley, P. A. Three-Dimensional Imaging of Localized Surface Plasmon Resonances of Metal Nanoparticles. *Nature* **2013**, *502*, 80.

[44] Bigelow, N. W.; Vaschillo, A.; Iberi, V.; Camden, J. P.; Masiello, D. J. Characterization of the Electron- and Photon-Driven Plasmonic Excitations of Metal Nanorods. *ACS Nano.* **2012**, *6* 7497-7504 (2012).

[45] Bigelow, N. W.; Vaschillo, A.; Camden, J. P.; Masiello, D. J. Signatures of Fano Interferences in the Electron Energy Loss Spectroscopy and Cathodoluminescence of Symmetry-Broken Nanorod Dimers. *ACS Nano.* **2013**, *7*, 4511-4519.

[46] Li, G.; Cherqui, C.; Bigelow, N. W.; Duscher, G.; Straney, P. J.; Millstone, J. E.; Masiello, D. J.; Camden, J. P. Spatially Mapping Energy Transfer from Single Plasmonic Particles to Semiconductor Substrates *via* STEM/EELS. *Nano Lett.* **2015**, *15*, 3465-3471.

[47] Zhang, Z.; Liu, T.; Smith, A. E.; Medhekar, N. V.; Nakashima P. N. H.; Bourgeois, L. Mechanisms of Void Shrinkage in Aluminium. *J. Appl. Crystal.* **2016**, *49*, 1459-1470.

[48] Muller, D. A.; Silcox, J. Delocalization in Inelastic Scattering. *Ultramicroscopy* **1995**, *59*, 195.

[49] Apell, S. P.; Echenique, P. M.; Ritchie, R. H. Sum Rules for Surface Plasmon Frequencies. *Ultramicroscopy* **1996**, *65*, 53-60.

[50] Kelly, K.; Coronado, E.; Zhao, L.; Schatz, G.. The Optical Properties of Metal Nanoparticles: The Influence of Size, Shape, and Dielectric. *J. Phys. Chem. B* **2003**, *107*, 668–677.

[51] Rodríguez-Fernández, J.; Novo, C.; Myroshnychenko, V.; Funston, A. M.; Sánchez-Iglesias, A.; Pastoriza-Santos, I.; Pérez-Juste, J.; García de Abajo F. J.; Liz-Marzán, L. M.; Mulvaney, P. Spectroscopy, Imaging and Modeling of Individual Gold Decahedra. *J. Phys. Chem. C* **2009**, *113*, 18623–18631.

[52] Kulcinski, G. L.; Brimhall, J. L.; Kissinger, H. E. Production of Voids in Nickel with High Energy Selenium Ions. *J. Nuclear Mater.* **1971**, *40*, 166-174.

[53] Mazey, D. J.; Francis, S.; Hudson, J. A. Observation of A Partially-Ordered Void Lattice in Aluminium Irradiated with 400 keV Al+ Ions. *J. Nuclear Mater.* **1973**, *47*, 137-142.

[54] Bradley, C. R. Argonne National Laboratory Report No. ANL-88-48, **1988**.

[55] Muller, D. A.; Silcox, J. Radiation Damage of Ni_3Al by 100 keV Electrons. *Phil. Mag. A.* **1995**, *71*, 1375-1387.

[56] Gloter, A.; Douiri, A.; Tencé M.; Colliex, C. Improving Energy Resolution of EELS Spectra: An Alternative to the Monochromator Solution. *Ultramicroscopy* **2003**, *96*, 385-400.

[57] Cowley, J. M.; Moodie, A. F. The Scattering of Electrons by Atoms and Crystals. I. A New Theoretical Approach. *Acta Cryst.* **1957**, *10*, 609-619.

[58] Nakashima, P. N. H.; Muddle, B. C. Differential Quantitative Analysis of Background Structure in Energy-Filtered Convergent-Beam Electron Diffraction Patterns. *J. Appl. Cryst.* **2010**, *43*, 280-284.

[59] Nakashima, P. N. H.; Muddle, B. C. Differential Convergent Beam Electron Diffraction: Experiment and Theory. *Phys. Rev. B* **2010**, *81*, 115135.

[60] Midgley, P. A. Electronic Bonding Revealed by Electron Diffraction. *Science* **2011**, *33*, 1528-1529.